



A Turbulence-Resolving Numerical Investigation of Wave-Supported Gravity Flows

Liangyi Yue¹ , Zhen Cheng^{2,3} , and Tian-Jian Hsu¹

¹Center for Applied Coastal Research, Civil and Environmental Engineering, University of Delaware, Newark, DE, USA, ²Applied Ocean Physics and Engineering, Woods Hole Oceanographic Institution, Woods Hole, MA, USA, ³Now at Convergent Science, Inc., Madison, WI, USA

Key Points:

- For typical bed slope and wave condition in the active margin, wave-supported gravity flows over flat bed are transitionally turbulent
- Simulated gravity flow has a speed of about 1 ~ 2 cm/s, and sediment mass concentration is no more than 30 kg/m³
- Wave direction can change the resulting gravity current speed by about a factor of 2

Correspondence to:

L. Yue,
liangyi@udel.edu

Citation:

Yue, L., Cheng, Z., & Hsu, T.-J. (2020). A turbulence-resolving numerical investigation of wave-supported gravity flows. *Journal of Geophysical Research: Oceans*, 125, e2019JC015220. <https://doi.org/10.1029/2019JC015220>

Received 12 APR 2019

Accepted 15 JAN 2020

Accepted article online 4 FEB 2020

Abstract Wave-supported gravity flows (WSGFs) have been identified as a key process driving the offshore delivery of fine sediment across continental shelves. However, our understanding on the various factors controlling the maximum sediment load and the resulting gravity current speed remains incomplete. We adopt a new turbulence-resolving numerical model for fine sediment transport to investigate the formation, evolution, and termination of WSGFs. We consider the simplest scenario in which fine sediments are supported by the wave-induced fluid turbulence at a low critical shear stress of erosion over a flat sloping bed. Under the energetic wave condition reported on the Northern California Coast with a shelf slope of 0.005, simulation results show that WSGFs are transitionally turbulent and that the sediment concentration cannot exceed 30 kg/m³ (g/L) due to the attenuation of turbulence by the sediment-induced stable density stratification. Wave direction is found to be important in the resulting gravity current intensity. When waves are in cross-shelf direction, the downslope current has a maximum velocity of 1.2 cm/s, which increases to 2.1 cm/s when waves propagate in the along-shelf direction. Further analysis on the wave-averaged momentum balance confirms that when waves are parallel to the slope (cross-shelf) direction, the more intense wave-current interaction results in larger wave-averaged Reynolds shear stress and thus in a smaller current speed. Findings from this study suggest that the more intense cross-shelf gravity current observed in the field may be caused by additional processes, which may enhance the sediment-carrying capacity of flow, such as the ambient current or bedforms.

Plain Language Summary Fine sediments delivered by rivers are the main agent to carry terrestrial organic carbon, nutrients, and contaminants to the deep ocean. Therefore, it is important to understand and further predict the fate of these fine sediments in the coastal ocean. Recent field observations have revealed that through resuspension by waves, the thin wave bottom boundary is a main offshore delivery pathway of fine sediment, through a process called wave-supported sediment-driven gravity flows. This study uses a turbulence-resolving numerical model for fine sediment resuspension in the wave bottom boundary layer to simulate the wave-supported gravity flows driven by energetic wave conditions that are observed in active margins. Model results allow us to provide a constraint on the maximum offshore sediment flux for flat bed condition, and the uncertainty due to wave direction is also addressed. Compared with field observations, findings from this model study indicate that other key factors, such as bedforms and superimposed currents, may play a role to enhance the offshore sediment flux.

1. Introduction

Identification of the physical processes driving substantial offshore transport of fine terrestrial sediments across the continental shelves is the key to the overall understanding and prediction of sediment source to sink (Wright & Nittrouer, 1995). Fine sediment transport in coastal ocean is driven by a variety of processes, such as tidal currents, wind-generated currents, circulation by density gradients, hypopycnal or hyperpycnal river plumes, turbidity currents, and wave bottom boundary layer (WBBL) flows (Nittrouer & Wright, 1994). Typical shelf currents are mostly directed parallel to the coast and hence are the main drivers of along-shelf sediment transport (Nittrouer & Wright, 1994), while the shelf slope is usually too mild to drive autosuspension turbidity currents. Field observations at Northern California Shelf near Eel River revealed that even during river flooding events, most sediments delivered directly from the river plume were deposited on the

inner shelf (Geyer et al., 2000). Therefore, the main mechanisms responsible for the offshore delivery of fine sediment have been associated with the resuspension by wave orbital motions (Harris & Wiberg, 2002; Wright & Friedrichs, 2006).

Our general understanding of wave-driven resuspension of sediments from the sea floor is due to wave stirring, and the resulting offshore transport is parameterized by wave energy gradient across the continental shelf (Harris & Wiberg, 2002). Field observations in STRATAFORM program further revealed the existence of wave-supported gravity flows (WSGFs) as a viable mechanism driving persistent offshore transport of fine sediment in the coastal ocean (Ogston et al., 2000; Traykovski et al., 2000). These flows have been observed to be a cross-shelf near-bed density current due to highly concentrated fine sediment suspension over a sloping bed. Because of the gentle slope of continental shelves, the resulting buoyancy anomaly confined in the thin WBBL near seabed can only drive a low speed cross-shelf current (several cm/s; see Traykovski et al., 2000, 2007). However, using a simple parameterization of WSGF, Scully et al. (2003) estimated that about 26% of fine sediment delivered by Eel River to the midshelf during flood season was through WSGF. By incorporating a WBBL module to model WSGF in the regional-scale ocean model ECOM-SED, Harris et al. (2005) further showed that when WSGF was neglected, their model cannot predict the observed midshelf depositional pattern at Eel River Shelf. Thus, clear understanding and better parameterization of WSGF are necessary for studying the offshore sediment transport.

Although the importance of WSGF has been recognized, the magnitude of the corresponding cross-shelf sediment transport and the physical parameters that control it remain unclear. A key uncertainty of the transport lies in the magnitude of the cross-shelf (downslope) gravity current speed. A literature survey suggests that, although WSGFs have been observed in many continental shelves (e.g., Hale & Ogston, 2015; Jaramillo et al., 2009; Traykovski et al., 2000, 2007, 2015), the cross-shelf current speed differs by several factors, ranging from a few to tens of cm/s. Moreover, different from typical turbidity current, field data show that WSGF requires persistent wave energy to generate sufficient fluid turbulence in the WBBL, which supports the suspended sediments (Hale & Ogston, 2015; Traykovski et al., 2000). There are many physical variables that can affect the dynamics of WSGF. In addition to the wave forcing and shelf slope, whose maximum values are widely reported by field observations (Traykovski et al., 2000), other variables, such as the ambient current (Ma et al., 2008) and bedforms (Traykovski et al., 2015), may have the capability to enhance the sediment-carrying capacity (maximum sediment load) of flow and the downslope gravity flow speed. Laboratory experiments also confirmed that, when only about 13% of very fine sand was present in mud, small bedforms appeared which enhance the wave boundary layer turbulence (Hooshmand et al., 2015).

There are several challenges to directly resolve WSGF in the regional-scale modeling of sediment source to sink. First, typical ocean models are formulated in terms of wave-averaged variables, and hence the intrawave processes are not resolved. As a result, a WBBL module or parameterizations for WSGF using the averaged momentum balance and equilibrium mass balance are needed (Harris et al., 2005; Scully et al., 2003; Wright et al., 2001). Second, field observations all indicate that WSGFs occur primarily in the WBBL, whose thickness is only about 10 cm. A way to obtain a better understanding of WSGF is to employ a turbulence-resolving model to gain insight into turbulence and fine sediment transport in the transitionally turbulent WBBL. At the most energetic condition where WSGFs have been observed, previous turbulence-resolving numerical simulations of sediment-laden WBBL (without a slope) indicated that the WBBL is transitionally turbulent, meaning that the flow is only turbulent during a portion of the wave period (Cheng et al., 2015; Ozdemir et al., 2010). Furthermore, it was found that the sediment-induced stable density stratification attenuated flow turbulence when a sufficient amount of fine sediment was available.

This caused the formation of a lutocline, a region of sharp negative sediment concentration gradient, which effectively confined fine sediments within the thin wave boundary layer, consistent with field observed WSGF events (Traykovski et al., 2000, 2015). More importantly, their simulation results showed that when enough sediments were introduced to WBBL (through either initially prescribed sediment load or resuspension from the bottom), the flow became laminar. In other words, at a given sediment settling velocity and wave intensity, there exists a maximum sediment load (or sediment-carrying capacity). Beyond this limit, turbulence in the wave boundary layer is significantly attenuated, and the flow becomes laminar. As a result, the WBBL can no longer sustain more sediments.

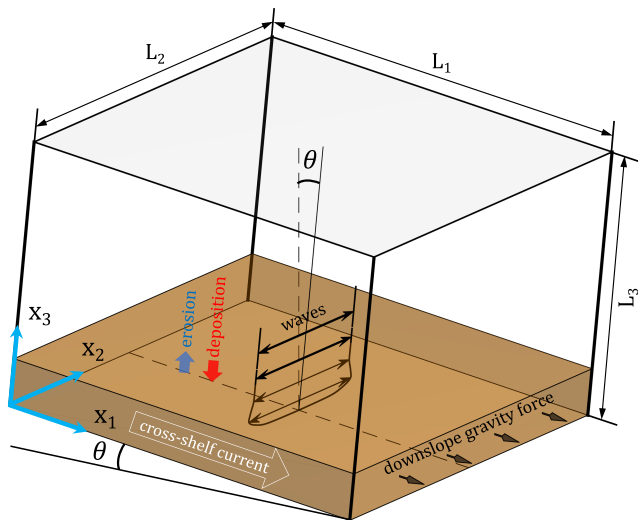


Figure 1. Sketch of computational domain and definition of the coordinate system.

Insights into sediment-laden WBBL by turbulence-resolving simulations can be extended to simulate WSGF by including a gentle bottom slope. Ozdemir (2016) showed that for a shelf slope of 0.005, the peak downslope velocity was achieved at the sediment-carrying capacity of flow but the value was only about 0.8 cm/s. Although this downslope velocity is lower than that observed in the field, Ozdemir (2016)'s work is important as its finding implies that other physical factors not investigated by his numerical model could enhance the downslope gravity current. In the model of Ozdemir (2016), the main control for the speed of downslope gravity flow is the prescribed constant suspended sediment load. In reality, the sediment load in WBBL is a variable dictated by bottom resuspension and deposition. In this study, we present a newly developed turbulence-resolving numerical model, which is able to efficiently simulate WSGFs with the sediment resuspension and deposition capability. To continue the work of Ozdemir (2016), we investigate the transitional turbulent flow features of WSGF and address the physical factor of wave direction in WSGF.

The goal of this study is to understand the intensity of WSGFs under the energetic wave conditions similar to Northern California continental shelf using a turbulence-resolving numerical model with a more realistic resuspension/deposition capability. The specific objectives are to (1) understand the transitional turbulent flow characteristics of the resulting WSGF over an erodible flat bed, (2) investigate the generation, evolution, and termination of WSGFs, particularly regarding the mechanics controlling the downslope gravity current, and (3) compare the simulation results with existing field observations and parameterizations in regional-scale modeling, in order to improve the understanding and modeling of WSGFs. The remainder of this paper is organized as follows. Model formulation, design of numerical experiments, and method used for data analysis are presented in section 2. Section 3 contains the main model results of WSGFs. Intrawave flow characteristics and transitionally turbulent flow features are shown in section 3.1. The resulting cross-shelf currents and sediment-laden WBBLs over a sloping bed are presented in section 3.2. The mechanism governing the downslope gravity driven flow in WSGF are studied in section 3.3. Discussions on the comparison with field observations and on the parameterization of WSGFs are given in section 4. Conclusions are given in section 5.

2. Methodology

2.1. Model Domain

As one kind of seafloor gravity currents, the WSGF is simplified in this study to be a WBBL problem using the boundary layer approximation, which is appropriate for relatively long surface wave with small amplitude (typical on continental shelf; Trowbridge & Madsen, 1984). An idealized computational domain covering the WBBL over an erodible flat bed (Figure 1) is used. In a coordinate system with its origin in the bottom corner, the rectangular domain has a size of $L_1 \times L_2 \times L_3$ in the downslope (or cross-shelf x_1), the cross-slope (or along-shelf x_2), and the bed-normal (x_3) directions, respectively. For numerical experiments of WSGF, the small bottom slope $\tan(\theta)$ is always specified in x_1 direction (illustrated in Figure 1).

The formation of WSGF is due to a significant amount of fine sediment suspended by the near-bed wave orbital motion, while the ambient current is relatively weak (Traykovski et al., 2000). In this work, we seek for a numerical solution of WSGF in statistically steady state under the energetic wave condition in the Northern California continental shelf near Eel River where WSGFs were observed. In our simulations, the boundary layer flow is driven by a time-oscillatory pressure gradient, which is uniform in the bed-normal direction. The resulting free-stream above the turbulent WBBL mimics the wave orbital motion caused by long waves, which is idealized to have a simple sinusoidal velocity. The intensity of oscillatory flow is uniquely characterized by the amplitude of free-stream velocity, while the wave direction is specified in either the cross- or along-shelf direction in order to investigate its effect on the resulting WSGFs.

In the resulting WBBL, the near-bed wave orbital motion exerts a shear stress on the erodible flat bed. When the bottom shear stress exceeds the critical shear stress of erosion, sediments are eroded and enter the computational domain. We assume that the sediments in suspension are monodispersed, which are supported

by the wave-induced fluid turbulence during WSGF events. Following the boundary layer approximation, the two-phase (water and sediment) flow is regarded to be statistically homogeneous in the cross-shelf (x_1) and along-shelf (x_2) directions, where periodic boundary conditions are implemented. For a given wave condition, the suspended sediment load is controlled by the resuspension and deposition of bed sediments (Cheng et al., 2015). Due to the relatively small settling velocity of fine sediment considered here, turbulence in the WBBL constantly suspends a considerable amount of sediment in the model domain.

According to earlier numerical studies of fine sediment transport in WBBL without a bottom slope (Cheng et al., 2015; Ozdemir et al., 2010), when enough sediments are suspended in the domain, the sediment suspension is confined within a thin layer close to the bed due to the sediment-induced stable density stratification. When the WBBL has a gentle bottom slope (specified in x_1 direction), the near-bed density anomaly caused by the sediment suspension creates a persistent gravitational force in the downslope direction, which drives a wave-averaged cross-shelf current (illustrated in Figure 1). The resulting WSGF reaches an equilibrium state when the downslope gravitational force balances the vertical distribution of the total shear stress in the water column (Parsons et al., 2009). Moreover, there exists a maximum sediment load for a given WBBL due to the significant attenuation of turbulence induced by sediment. Consequently, the cross-shelf gravity current has a maximum speed when the suspended sediment load reaches the carrying capacity of flow. We design numerical experiments in section 2.4 to investigate this maximum current speed.

2.2. Governing Equations and Boundary Conditions

2.2.1. The Two-Phase Flow Eulerian Method

The equilibrium Eulerian approach (Balachandar & Eaton, 2010) has been widely used in the study of dilute fine sediment transport (Cheng et al., 2015; Ozdemir et al., 2010; Shringarpure et al., 2012). Under the assumption that the fine sediment particles in water have negligible inertia, the suspended sediments can follow the local carrier flow closely (Ferry et al., 2003). Consequently, the velocity field of sediment phase v_i is determined from the velocity field of carrier flow u_i and the particle settling velocity w as

$$v_i = u_i + wn_i. \quad (1)$$

For clarity, tensor notation is utilized hereafter and the subscript $i = 1, 2, 3$ corresponds to the downslope (cross-shelf), cross-slope (along-shelf), and bed-normal directions, respectively. In equation (1), n_i is a normalized gravity vector representing the direction of the gravitational acceleration. In the adopted coordinate system (see Figure 1), it reads $n_i = [\sin \theta, 0, -\cos \theta]$. The application of the equilibrium Eulerian approximation simplifies the full Eulerian two-phase flow formulation by avoiding solving the particle momentum equations.

2.2.2. Fluid Phase

For dilute sediment transport in water, the Boussinesq approximation is valid to simplify the governing equations for carrier flow phase. Subject to the continuity equation $\partial u_i / \partial x_i = 0$, the incompressible Navier-Stokes momentum equations for carrier flow read (Shringarpure et al., 2012)

$$\frac{\partial u_i}{\partial t} + u_j \frac{\partial u_i}{\partial x_j} = -\frac{1}{\rho} \frac{\partial p}{\partial x_i} + \nu \frac{\partial^2 u_i}{\partial x_j \partial x_j} + Rg\phi n_i + S_i, \quad (2)$$

where ρ is the water density, ν is the fluid kinematic viscosity, g is the gravitational acceleration constant, $R = 1.65$ is the submerged specific gravity of sediment, p is the pressure field, and ϕ denotes the volumetric concentration of sediment. In equation (2), the buoyancy (third) term on the right-hand side (RHS) accounts for the coupling effects from sediment phase. The last term S_i represents the prescribed time-variant pressure gradients for the generation of oscillatory flows, which is written as

$$S_i = U_w \Omega_w \cos(\varphi) m_i, \quad (3)$$

where U_w is the amplitude of free-stream velocity, $\Omega_w = 2\pi/T_w$ is the wave angular frequency with T_w representing the wave period, $\varphi = \Omega_w t$ is the wave phase, and m_i (see Table 1) is the wave direction vector. By using equation (3), the free-stream orbital motion is expressed as a monochromatic and perfectly symmetric time series of $u_w(t) = U_w \sin(\varphi)$. In this study, we simulate the same wave condition with different wave directions specified by m_i , while the bottom slope is fixed in the x_1 (cross-shelf) direction.

Table 1

A List of Simulations Investigated in This Study

Case	θ (rad)	m_i^a	$L_1 \times L_2 \times L_3$ (Δ)	$N_1 \times N_2 \times N_3$	$N_w^b(T_w)$
0	0	[1, 0, 0]	$60 \times 30 \times 60$	$256 \times 192 \times 193$	60
1	0.005	[1, 0, 0]	$60 \times 60 \times 60$	$256 \times 256 \times 193$	60
2	0.005	[0, 1, 0]	$60 \times 60 \times 60$	$256 \times 256 \times 193$	60

^a m_i represents the direction of waves while the bottom slope is fixed in the x_1 direction. ^b N_w is the total run time of simulation in units of wave period.

The computational domain has a shear-free top boundary where the free-slip, rigid-lid boundary condition is implemented, which reads

$$\frac{\partial u_1}{\partial x_3} = 0, \frac{\partial u_2}{\partial x_3} = 0, u_3 = 0 \quad \text{at } x_3 = L_3. \quad (4)$$

Due to this free-slip treatment at top of the domain, the entrainment of ambient fluid leads to a slow development in the wave-averaged current above the lutocline where flow is nearly laminar (Shringarpure et al., 2012). However, this slow increase in mean current above the lutocline almost has no impact on the near-bed gravity flow, and its effect is assumed to be negligible. In contrast, the bottom of the computational domain is modeled as an erodible bed, and the no-slip boundary condition is applied for the fluid velocities, which is written as

$$u_i = 0 \quad \text{at } x_3 = 0. \quad (5)$$

2.2.3. Sediment Phase

Derived from the principle of mass conservation, the resulting advection-diffusion equation for the volumetric concentration of sediment is written as (Shringarpure et al., 2012)

$$\frac{\partial \phi}{\partial t} + \frac{\partial (\phi v_j)}{\partial x_j} = K \frac{\partial^2 \phi}{\partial x_j \partial x_j}, \quad (6)$$

where K is the effective diffusivity of sediment. Similar as in previous studies (Cheng et al., 2015; Ozdemir et al., 2010), the Schmidt number $Sc = \nu/K$ is specified to be 0.5. Note that the sediment phase velocity v_j is calculated using equation (1) from the carrier flow velocity and the particle settling velocity.

For the sediment phase, the no-flux boundary condition is applied at the top of the domain. This condition imposes no net transport of sediment across the top boundary throughout the computation, which reads (Ozdemir et al., 2010)

$$\phi w n_3 - K \frac{\partial \phi}{\partial x_3} = 0 \quad \text{at } x_3 = L_3. \quad (7)$$

At the bottom of the computational domain, the erodible/depositional boundary condition (Cheng et al., 2015; Nelson & Fringer, 2018) is implemented, which is written as

$$\phi w n_3 - K \frac{\partial \phi}{\partial x_3} = q_e + q_d \quad \text{at } x_3 = 0, \quad (8)$$

Table 2

A Summary of Key Averaged Flow Quantities for Simulations Investigated in This Study

Case	$M^a(T_w)$	$\langle \tau_b \rangle_c$ (Pa)	Ri^b	\bar{F}_g (g/cm ² s)	\bar{U}_{gf} (cm/s)
0	20	0.42	1.58×10^{-4}	—	—
1	20	0.43	1.63×10^{-4}	4.68×10^{-3}	0.93
2	20	0.43	1.64×10^{-4}	7.94×10^{-3}	1.66

^a M is the number of wave periods to the end of simulation where the data analysis is taken. ^bThe bulk Richardson number is defined as $Ri = Rg\Delta\Phi/U_w^2$, which quantifies the sediment-induced density stratification (Ozdemir et al., 2010).

where q_e and q_d are the erosional and depositional fluxes at the bottom, respectively. Following the continuous deposition formulation (Sanford, 2008), the depositional flux is modeled as $q_d = \phi \omega n_3$. Since the sediment concentration ϕ is calculated in every numerical time step, the depositional flux is a model variable depending on the last flow condition in the domain. The erosional flux is calculated using the Partheniades-Ariathurai-type formulation (Sanford & Maa, 2001), which has the following expression

$$q_e = \begin{cases} m_e \left(\frac{|\tau_b|}{\tau_c} - 1 \right) & \text{for } |\tau_b| \geq \tau_c \\ 0 & \text{for } |\tau_b| < \tau_c \end{cases}, \quad (9)$$

where m_e is an empirical erosion rate, τ_c is the critical bottom shear stress of erosion, $\tau_b = \rho \nu \left[\partial u_1 / \partial x_3, \partial u_2 / \partial x_3 \right]_{x_3=0}$ is the bottom shear stress, and $|\tau_b|$ denotes its magnitude. Based on $|\tau_b|$, the friction velocity is calculated as $u_* = \sqrt{|\tau_b| / \rho}$. According to equation (9), the erosional flux is a function of time and space.

2.3. Implementation

A new numerical modeling system is built based on the theoretical formulation described in section 2.2. This section provides a brief overview of the numerical schemes, and more details are given in Yue et al. (2019). The governing equations (2) and (6) are advanced in time sequentially by a third-order low-storage Runge-Kutta scheme (Williamson, 1980), and the Courant-Friedrichs-Lewy condition is implemented to limit the size of a time step with a maximum Courant-Friedrichs-Lewy number of 0.5. Applying the pseudospectral scheme following Cortese and Balachandar (1995), the momentum equations (2) of the carrier flow phase are numerically solved with the corresponding boundary conditions (equations (4) and (5)). During each of the three time levels in a computational step, the standard two-stage (predictor and corrector) projection method (Chorin, 1968) is utilized to enforce a divergence-free velocity field of the carrier flow. Right after the velocity projection for the carrier flow phase, the sediment volumetric concentration is computed by solving equation (6) in a way similar to the predictor stage of carrier flow with the boundary conditions (7) and (8).

The computational domain (Figure 1) is spatially discretized with a grid number of $N_1 \times N_2 \times N_3$ in the downslope, cross-slope, and bed-normal directions, respectively. In the horizontal directions, the grid spacings are uniform, and the discrete Fourier transform (DFT) is implemented in these two directions, which enforces the corresponding periodic boundary conditions. On the contrary, grid spacing is nonuniform in bed-normal direction, and the Chebyshev-Gauss-Lobatto points are used. For the advection terms in equations (2) and (6), the Arakawa scheme (Arakawa & Lamb, 1981) is utilized, and the classical 3/2 rule is applied to remove the aliasing errors (Canuto et al., 1988). The semi-implicit second-order Crank-Nicolson method is implemented for the diffusion terms. After the application of the matrix multiplication technique (Peyret, 2002), the governing equations are represented by a set of Helmholtz equations in wavenumber domain, which are directly solved by using the matrix-diagonalization method (Peyret, 2002).

Functioned by the Message Passing Interface technique, the modeling system implements the two-dimensional (2-D) pencil decomposition of the computational domain (Pekurovsky, 2012) in the horizontal directions for parallel computing. Through several standard benchmark tests, the newly built modeling system used in this study is carefully verified in Yue et al. (2019).

2.4. Experiments

Numerical simulations with a free-stream velocity amplitude of $U_w = 0.56$ m/s and a wave period of $T_w = 10$ s are carried out in this study. This corresponds to a Stokes boundary layer thickness of $\Delta = \sqrt{2\nu/\Omega_w} = 1.8 \times 10^{-3}$ m and the resulting Stokes Reynolds number $Re_\Delta = U_w \Delta / \nu = 1,000$. According to earlier studies on transitional turbulence in WBBL (Jensen et al., 1989; Vittori & Verzicco, 1998), a WBBL with $Re_\Delta = 1,000$ is in the intermittently turbulent regime, where the flow is turbulent only in part of a wave cycle. Following Ozdemir et al. (2010), we specify a constant settling velocity of sediment of $w = 5.0 \times 10^{-4}$ m/s, and the flocculation process (Soulsby et al., 2013) is ignored. Both the wave condition and settling velocity are similar to the energetic WSGF events observed in Eel River Shelf (Traykovski et al., 2000). The erodible bed has a critical bottom shear stress of erosion of $\tau_c = 0.025$ Pa and an empirical erosion rate of $m_e = 3 \times 10^{-7}$ m/s. With the given wave condition and settling velocity, these bed erodibility parameters allow for a suspended sediment load close to the flow carrying capacity (Cheng et al., 2015).

In order to reach our research objectives (section 1), three different numerical experiments are taken in this study with a summary of them listed in Table 1. Initialized with the flow fields from the corresponding quasi-steady clear-flow runs (Yue et al., 2019), simulations start with zero sediment concentration in the computational domain. For the generation of downslope gravity flows, we specify a gentle bottom slope of 0.005 in Case 1 and Case 2, which is in range of the commonly observed values on the active margin of continental shelves. Moreover, wave direction is regarded to be an uncertainty in WSGF by the present study. It is generally believed that during WSGF events, wave direction is primarily parallel to the shelf slope (Scully et al., 2002; Wright et al., 2001; Wright & Friedrichs, 2006). However, since the local wave direction also depends on other factors, such as wind direction and bathymetry, the corresponding WSGF dynamics due to wave direction need to be understood. Here, we quantify the variability due to wave direction by carrying two comparative runs between Case 1 and Case 2, where the waves are specified to be parallel and perpendicular to the downslope direction, respectively (Table 1). For the purpose of comparison, the simulation of Case 0 is also taken where the wave direction is in the x_1 direction and the bottom slope is set to be 0.

Field data suggest that once a WSGF is generated, it requires constant energy input from waves to maintain sediment suspension in the WBBL and the WSGF no longer exists when the wave motion is too weak (Hale & Ogston, 2015; Traykovski et al., 2000). Therefore, the termination of WSGF, particularly regarding the requirement of sustaining wave motion as reported in the field observations, has to be reproduced by the present numerical simulation. Simulations of Case 1 and Case 2 are continued for another 20 wave periods from time $t_0 = 60T_w$ but with a dampened wave forcing, which is written as

$$S_i = U_w [\Omega_w \cos(\varphi) + \gamma \sin(\varphi)] \exp[\gamma(t - t_0)] m_i, \quad (10)$$

where the parameter γ is the damping rate. Note that the termination of WSGF in field during the waning stage of a storm could be more complicated than that described by equation (10).

For numerical simulations of WSGF presented in this study (Case 1 and Case 2), the computational domain has a size of $60\Delta \times 60\Delta \times 60\Delta$, which is confirmed to be large enough by computing the two-point correlation functions (Kim et al., 1987). This domain size is among the largest in the literature of simulating WBBL at Stokes Reynolds number $Re_\Delta = 1,000$ (Vittori & Verzicco, 1998). Our choice of domain size ensures that the largest turbulent eddy in an oscillatory boundary layer is contained in the computational domain. The domain is discretized with $256 \times 256 \times 193$ grid points in the two horizontal and bed-normal directions, respectively. The resulting grid resolution has been demonstrated to be fine enough for the study of fine sediment transport in the WBBL (Cheng et al., 2015; Ozdemir et al., 2010). As we will discuss later in section 3, the presence of the weak downslope gravity current has little effect on the strength of flow turbulence. Moreover, based on the peak friction velocity, this grid yields a resolution in wall unit of $\delta x_1^+ = \delta x_2^+ = 11.8$. In the bed-normal direction, we obtain $\delta x_3^+ = 0.2$ close to the wall and $\delta x_3^+ = 24.8$ in the middle of the water column. This grid resolution is similar to the one used in Ozdemir et al. (2010).

2.5. Variable Decomposition and Notation

The problem investigated in this study involves turbulent flow generated by wave motions and the wave-averaged current driven by downslope gravity. We adopt the triple decomposition method (Reynolds & Hussain, 1972) to isolate the weak downslope gravity current and the organized variations in the turbulent fluctuating flow field. The triple decomposition is applied in a similar manner as other turbulence-resolving numerical studies for a current-wave-fluctuation decomposition (Nelson & Fringer, 2018). We decompose a variable ψ into a current component $\langle \psi \rangle_c$, a wave component $\langle \psi \rangle_w$, and a fluctuating component ψ' as follows

$$\psi = \langle \psi \rangle_c(x_3) + \langle \psi \rangle_w(x_3; t) + \psi'(x_1, x_2, x_3; t). \quad (11)$$

To calculate each component shown in equation (11), we define the time- and phase-averaged components of a variable $\psi(x_1, x_2, x_3; t)$, respectively, as

$$\bar{\psi} = \frac{1}{MT_w} \int_{M_1 T_w}^{M_2 T_w} \psi(x_1, x_2, x_3; t) dt, \quad (12)$$

$$\langle \psi \rangle_p = \frac{1}{M} \sum_{n=0}^{M-1} \psi(x_1, x_2, x_3; t + nT_w), \quad (13)$$

where $M = M_2 - M_1$ is the number of wave periods in time range $[M_1 T_w, M_2 T_w]$ during which the data analysis is taken. Corresponding to the definition of time average (equation (12)), the average operation over a spatial dimension is written as

$$\langle \psi \rangle_i = \frac{1}{L_i} \int_0^{L_i} \psi(x_1, x_2, x_3; t) dx_i. \quad (14)$$

Consequently, we approximate the current component $\langle \psi \rangle_c$ by the time- and plane-averaging of the variable, namely,

$$\langle \psi \rangle_c = \langle \bar{\psi} \rangle_{12}. \quad (15)$$

The wave component $\langle \psi \rangle_w$ is then extracted by subtracting the current component $\langle \psi \rangle_c$ from the phase- and plane-averaged quantity $\langle \psi \rangle_{p12}$ as

$$\langle \psi \rangle_w = \langle \psi \rangle_{p12} - \langle \psi \rangle_c. \quad (16)$$

After obtaining the wave and current components, the turbulent fluctuating component ψ' is computed as

$$\psi' = \psi - \langle \psi \rangle_c - \langle \psi \rangle_w = \psi - \langle \psi \rangle_{p12}. \quad (17)$$

The notation defined here is particularly useful to present the statistically averaged quantities. Note that the average operations defined in equations (12)–(14) are commutative. As a result, the combination of multiple average operations can be denoted by the subscripts of the average operator “ $\langle \rangle$,” except for the time average. Accordingly, the turbulence kinetic energy (TKE) is defined as $k = \langle u'_i u'_i \rangle_{p12} / 2$, and the expression $\Phi = \langle \phi \rangle_{123}$ represents the domain-averaged sediment concentration. We denote $c = (1 + R)\rho\phi$ as the sediment mass concentration and $F_g = \langle f_g \rangle_{123}$ as the domain-averaged mass transport rate of sediment in the downslope direction, where $f_g = cu_1$ is the downslope sediment mass flux. Then, the ratio of sediment transport rate to the domain-averaged mass concentration is used to quantify the bulk gravity current speed, which reads

$$U_{gf} = \frac{F_g}{\langle c \rangle_{123}}. \quad (18)$$

3. Results

3.1. Intrawave Evolution of Near-Bed Dynamics

3.1.1. Bottom Shear Stress and Suspended Sediment

The temporal evolution of the domain-averaged sediment concentration and the downslope current speed illustrates the formation and development of WSGF (Figure 2). As shown in Figure 2b, for all the three cases, the domain-averaged sediment concentrations start to increase rapidly within the first 10 waves, and the equilibrium values are attained at about the 20th wave period. As more sediments are suspended into the domain, the sediment depositional (downward) flux near the bed also increases. In the incipient stage, the plane- and wave-averaged net erosion-deposition rate ($q_n = q_e + q_d$) of sediment at the bed is of order 10^{-5} m/s, which drops to 10^{-8} m/s after 20 wave periods. In other words, the averaged depositional flux balances with the erosional flux after the incipient stage and the amount of sediment in suspension quantified by the domain-averaged sediment concentration is in equilibrium. Wave direction shows negligible effect on the domain-averaged sediment concentration at equilibrium, although slightly lower Φ is found for Case 0 in which there is no bottom slope.

For cases with a mild bottom slope of 0.005, the suspended sediments drive downslope gravity currents and their temporal evolutions are illustrated by carrying out time average of the bulk gravity current speed (equation (18)) over every 10 wave periods (Figure 2c). In Case 2, where the waves are perpendicular to the bottom slope, the development of the downslope gravity current speed directly correlates with the amount of sediment in suspension (compare Figures 2b and 2c). During the incipient stage, as more sediments are suspended over the sloping bed, they start to drive a downslope current whose speed reaches its equilibrium value of around 1.66 cm/s (Table 2) after about 30 wave periods. When waves are in the same direction with respect to the bottom slope (Case 1), we observe a notably weaker downslope gravity current, reaching about 0.93 cm/s after 40 wave periods.

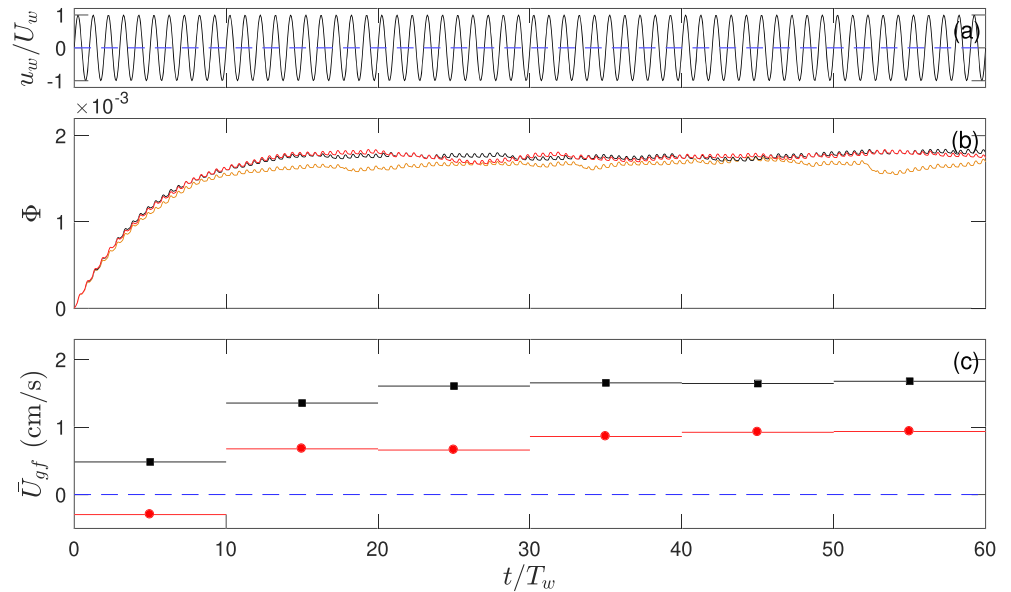


Figure 2. Time evolution of the (a) free-stream velocity; (b) domain-averaged volumetric concentration of sediment; and (c) flux-based downslope current speed for Case 0 (brown line), Case 1 (red lines), and Case 2 (black lines). Blue dashed lines are plotted to indicate 0 for reference.

Figure 3 shows the time evolution of the free-stream velocity, the phase-plane-averaged magnitude of bottom shear stress $\langle |\tau_b|_{p12} \rangle$ and phase-domain-averaged sediment concentration $\langle \phi \rangle_{p123}$ (phase-averaging over the 40th to 60th waves, see Table 2). This figure reveals that, all three cases show similar intrawave evolution of bottom shear stress, suggesting that the effects of mild bottom slope and wave direction are small. In each of the cases, there is an almost continuous erosion of sediment (upward erosional flux) since the bottom shear stress magnitude is greater than the critical shear stress of erosion of 0.025 Pa in more than 96% of a wave period (Figure 3b). These bottom shear stress time series are contrasted with the analytical solution of laminar flow (Jensen et al., 1989) in order to illustrate the intermittently turbulent flow features. During the first acceleration stage between $\varphi = 0$ and $2\pi/6$, bottom shear stresses of the three cases are close to the laminar solution and in particular, the well-known phase lead of $\pi/4$ (Cheng et al., 2015) is matched. Immediately after $\varphi = 2\pi/6$, the bottom shear stresses deviate from the laminar solution and increase rapidly to reach their peak values of about 0.85 Pa at around the wave crest of $\varphi = 3\pi/6$. During the deceleration stage between $\varphi = 3\pi/6$ and $6\pi/6$, the bottom shear stresses decrease quickly to 0 before the flow reversal ($\varphi = 6\pi/6$). The intrawave evolution of bottom shear stress observed here for cases with a mild slope are typical of transitionally turbulent WBL flow at this Reynolds number (Ozdemir et al., 2010; Vittori & Verzicco, 1998).

In contrast to the bottom shear stresses, the domain-averaged sediment concentrations show much lower temporal variability throughout the wave cycle (Figure 3c). The ratio of the sediment settling velocity to the bed friction velocity is used to quantify the importance of settling effect versus turbulent suspension. Based on the averaged amplitude of bottom shear stress $\langle |\tau_b| \rangle_c = 0.43$ Pa (Table 2), the averaged bed friction velocity is calculated as 2.07 cm/s. The fact that the settling velocity of sediment used in this study is only 5×10^{-4} m/s, the ratio of settling velocity to friction velocity has an averaged value of 2.41×10^{-2} , which is much smaller than unity. In other words, the turbulent suspension dominates the settling effect of sediment. Thus, similar amount of sediment is suspended in the computational domain without significant temporal change. Nevertheless, a notable increase of sediment concentration is still observed around the burst of bottom shear stress. We also find that adding a small bottom slope only slightly increases the bottom shear stress and thus the suspended sediment load (by about 3%), while the effect of wave direction on domain-averaged sediment concentration is almost negligible (Figure 3c).

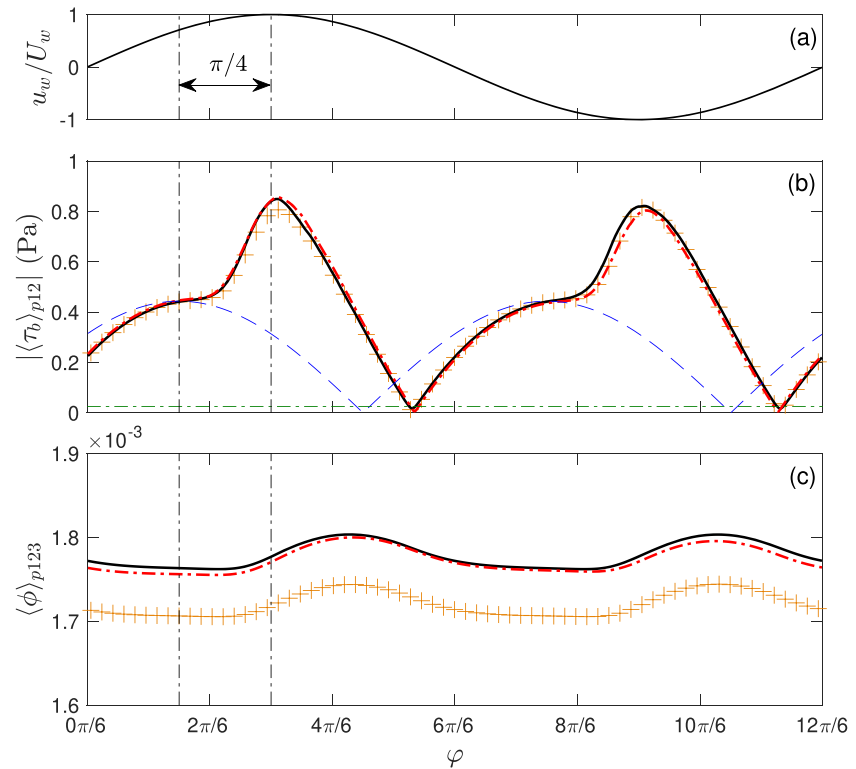


Figure 3. Time evolution of the (a) free-stream velocity; (b) amplitude of bottom shear stress; and (c) domain-averaged volumetric concentration of sediment for Case 0 (brown crosses), Case 1 (red dash-dotted lines), and Case 2 (black lines). The blue dashed line in subplot (b) is the corresponding laminar solution, while the green dash-dotted line represents the critical bottom shear stress.

3.1.2. Transitionally Turbulent Feature of WSGF

The present turbulence-resolving simulation results provide an opportunity to examine the transitionally turbulent feature of WSGF, through the visualization of coherent turbulent structures during the acceleration (Figure 4) and deceleration (Figure 5) instants.

Using Case 2 as an example, we apply the criterion of swirling strength λ_{ci} (Zhou et al., 1999), which represents the local fluid rotation speed, to visualize coherent turbulent structures. At $\varphi = 0$ and $\pi/6$, larger but weaker coherent turbulent structures are elevated from the bed. Interestingly, isosurface of λ_{ci} at $\varphi = 2\pi/6$ shows very high spatial variability with a portion of the domain ($x_1 = 0 \sim 40\Delta$) almost having no λ_{ci} exceeding the corresponding isovalue compared to other portion of the domain ($x_1 = 40\Delta \sim 60\Delta$). On the other hand, much more intense coherent turbulent structures at $\varphi = 3\pi/6$ and $4\pi/6$ are of smaller size and very densely populated close to the bed. The features of coherent turbulent structure (and intensity) are distinctly different between just a short time interval of $\varphi = 2\pi/6$ and $3\pi/6$, which is consistent with the time series of bottom shear stress discussed in Figure 3b. Moreover, consistent with the fine sediment assumption (section 2.2.1), the isosurfaces of sediment concentration generally respond directly to the coherent turbulent structures throughout a wave cycle, which is especially evident at $\varphi = 2\pi/6$.

Figure 6 presents the plane- and phase-averaged profiles of the streamwise flow velocity, the suspended sediment concentration, and the TKE at phase of the lowest ($\varphi = \pi/6$) and the highest ($\varphi = 3\pi/6$) turbulence intensity for Case 2. Although the magnitude of TKE intensity increases evidently from $\varphi = \pi/6$ to $\varphi = 3\pi/6$ (Figures 6c and 6f), the sediment concentration only increases slightly (Figures 6b and 6e). More importantly, both concentration profiles show the feature of a sharp negative sediment concentration gradient, called the lutocline, located around $x_3 = 15.5\Delta$. As discussed in previous studies (Cheng et al., 2015; Ozdemir et al., 2010), the formation of lutoclines is a prominent feature resulting from the sediment-induced stable density stratification, which attenuates fluid turbulence. Consequently, a remarkable amount of suspended sediment load is persistently confined between $x_3 = 0$ and $x_3 = 20\Delta$ (about 3.6 cm), having sufficient buoyancy anomaly to further drive a downslope gravity flow (section 3.2). From the intensity of TKE, the

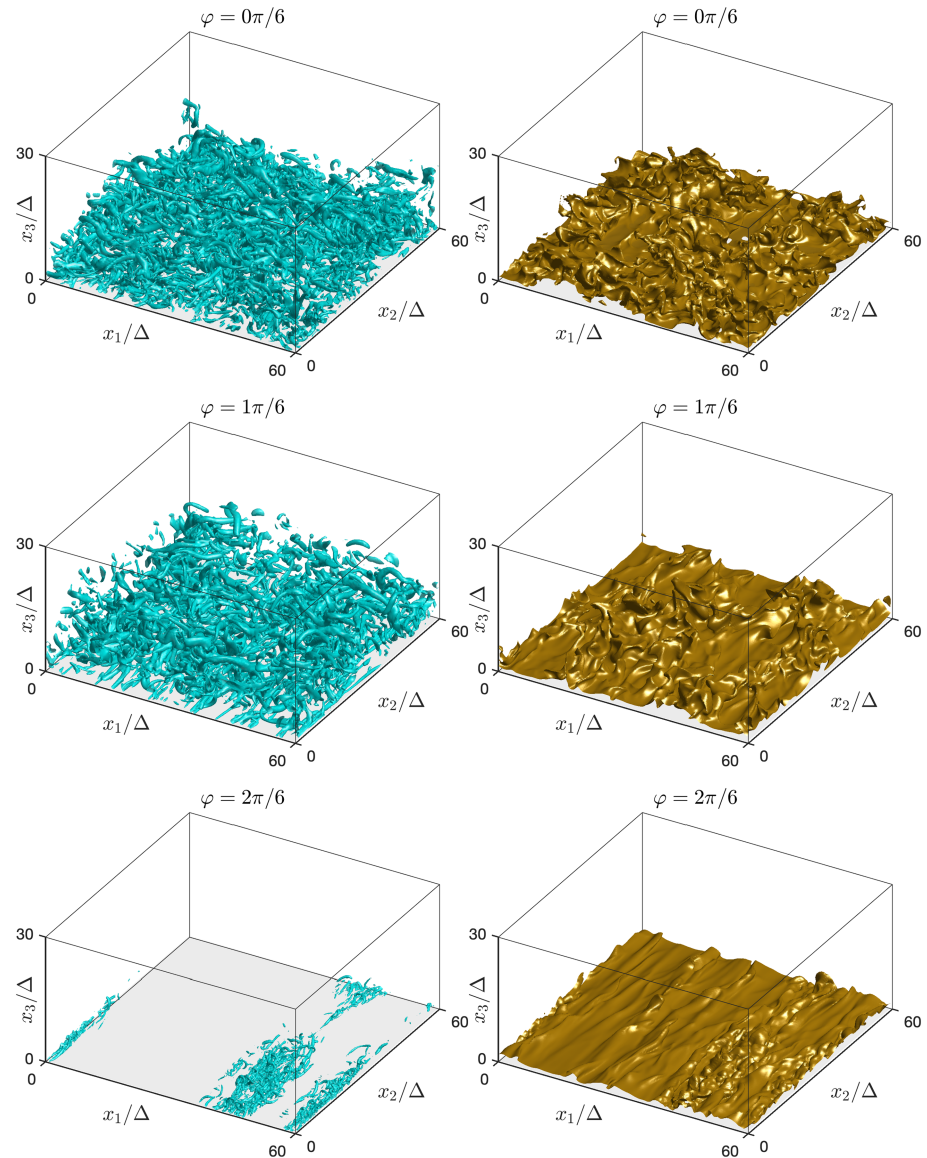


Figure 4. Coherent turbulent structures of flow (left column) and corresponding isosurfaces of near-bed sediment concentration (right column) of Case 2 at wave phases $\varphi = 0\pi/6$, $1\pi/6$, and $2\pi/6$. The coherent turbulent structures are visualized using the swirling strength (λ_{ci}), where the contour levels are set to be 10% of the corresponding maximum values with $\max(\lambda_{ci}) = 13.92$, 10.01 and 57.39 for the three phases, respectively. The contour levels of sediment concentration are chosen to be the averaged values at position $x_3 = 1.5$, which are 7.72×10^{-3} , 7.55×10^{-3} , and 7.80×10^{-3} , respectively.

transitional characteristics of flow discussed in Figures 4 and 5 are confirmed. At $\varphi = \pi/6$, the turbulence is more than 10 times weaker than that under the wave crest at $\varphi = 3\pi/6$, implying an evident change in level of turbulence during the intrawave evolution.

3.2. Gravity Currents on Gentle Bottom Slope

The intrawave results presented in section 3.1 confirm that the transitionally turbulent WBBL has a two-layer like structure and persistently suspends sediment within a few centimeters above the bed throughout a wave cycle. When a gentle bottom slope presents in the sediment-laden WBBL (Case 1 and Case 2), the resulting downslope gravitational force caused by the near-bed density anomaly from sediment suspension can drive an offshore-directed gravity flow. This important gravity flow process is presented in this section, which relates to the research objective 2).

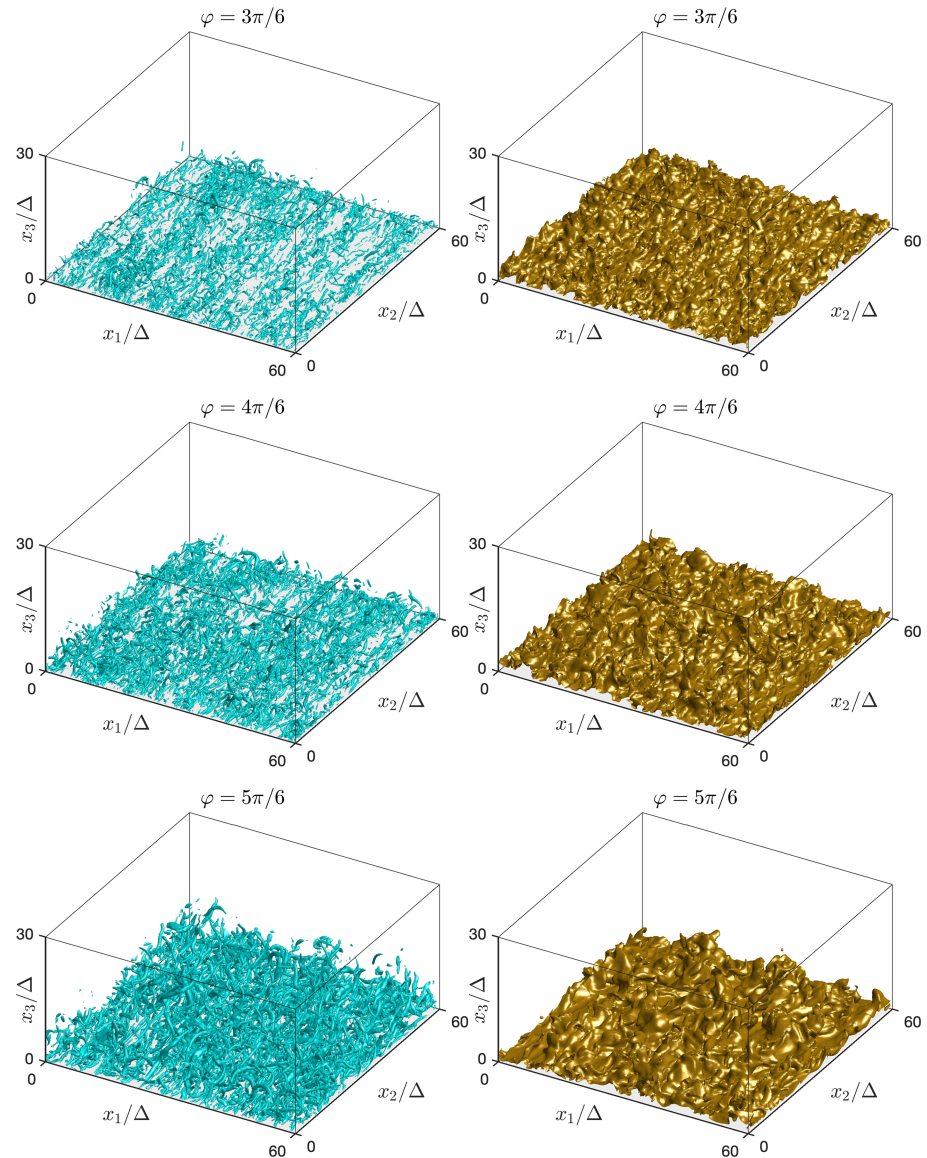


Figure 5. As Figure 4, but at wave phases $\varphi = 3\pi/6$, $4\pi/6$, and $5\pi/6$. For the three phases, the maximum swirling strength are $\max(\lambda_{ci}) = 89.12$, 57.98 , and 29.00 , while the contour levels of sediment concentration are 8.34×10^{-3} , 8.37×10^{-3} , and 8.06×10^{-3} , respectively.

3.2.1. Downslope Current and Sediment Transport

To facilitate the comparison with other field and model studies, we present model results in this section using sediment mass concentration c . The time- and plane-averaged (over the last 20 wave periods, see Table 2) vertical profiles of the sediment mass concentration $\langle c \rangle_c$, the downslope current velocity $\langle u_1 \rangle_c$, the downslope sediment mass flux $\langle f_g \rangle_c$, and the TKE (k) for the three cases are shown in Figure 7. Averaged sediment concentration profiles are similar for all three cases, particularly regarding the formation of the lutocline and the two-layer like structure (Figure 7a). The close similarity in concentration profiles is consistent with the almost identical TKE profiles shown in Figure 7d, since sediments are primarily suspended by turbulence. Moreover, sediments in suspension are constrained in a layer close to the bottom.

To be specific, more than 91% of the suspended sediments are below the lutocline (defined as the inflection point of sediment concentration profile) which is located at $x_3 = 2.82$ cm, while the height of the computational domain is $L_3 = 10.70$ cm. Right above the bed, the mass concentration of sediment reaches about 26 kg/m^3 (g/L). This amount of suspended load indeed drive an offshore-directed gravity current over the gentle bottom slope of 0.005 specified here (Figure 7b). In both Case 1 and Case 2, the mean current profiles

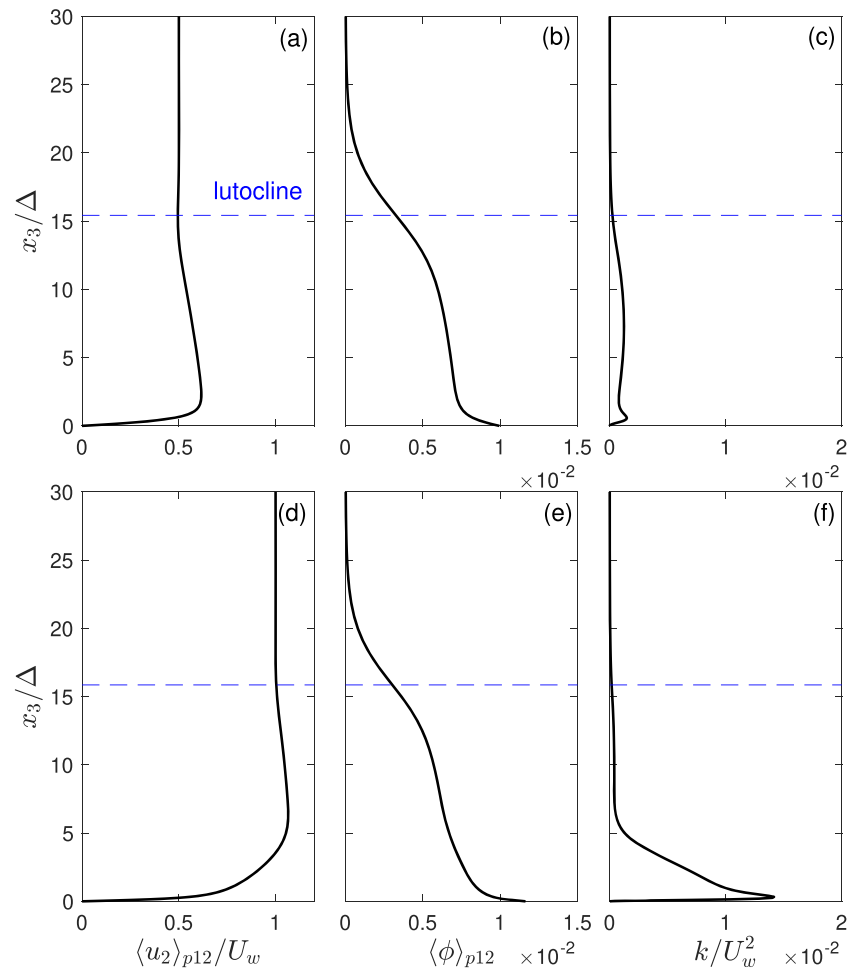


Figure 6. Plane- and phase-averaged (a, d) velocity in the direction of the waves; (b, e) volumetric concentration of sediment; (c, f) turbulence kinetic energy of flow for Case 2. Subplots in the first and second rows represent results at wave phase $\varphi = \pi/6$ and $3\pi/6$, respectively.

increase from 0 at the bed to their peak values near the location of lutocline. Moving upward, the currents decrease slowly to the top of the computational domain. The offshore currents, along with the suspended sediment, cause the corresponding offshore sediment fluxes, whose profiles have their maximums located in the middle of the sediment layer (Figure 7c). Hence, it is clear that these offshore currents are associated with the near-bed suspended sediment load.

One important feature to be noted is that, while the sediment concentration and TKE profiles are nearly identical in Case 1 and Case 2, the resulting intensity of downslope gravity current and thus the sediment transport are clearly dependent on the wave direction. Specifically, for Case 1 with waves parallel to the downslope direction, the offshore-directed current is weaker and has a peak downslope velocity of 1.2 cm/s. This value increases to 2.1 cm/s in Case 2 when waves are perpendicular to the slope direction. In addition, the maximum of offshore sediment mass flux of Case 2 is larger than that of Case 1 by a factor of 1.57.

Although WSGFs require constant support from wave-induced fluid turbulence in WBBL and thus are considered fundamentally different from typical turbidity currents (Parsons et al., 2009), there are still some similarities between these two sediment-driven gravity flows. Similar to turbidity current, the vertical structure of the mean velocity profiles in WSGFs obtained here consists of two regions. As expected for the conventional turbulent boundary layer, there is an inner region approximately below the lutocline where the gradient of velocity is positive (Figure 7b). This region contains the majority of sediment load (Figure 7a) where more than 90% of the sediment transport occurs in the present cases (Figure 7c). In contrast, an outer region is defined above the inner region where the velocity gradient is negative. Clearly from Figure 7b,

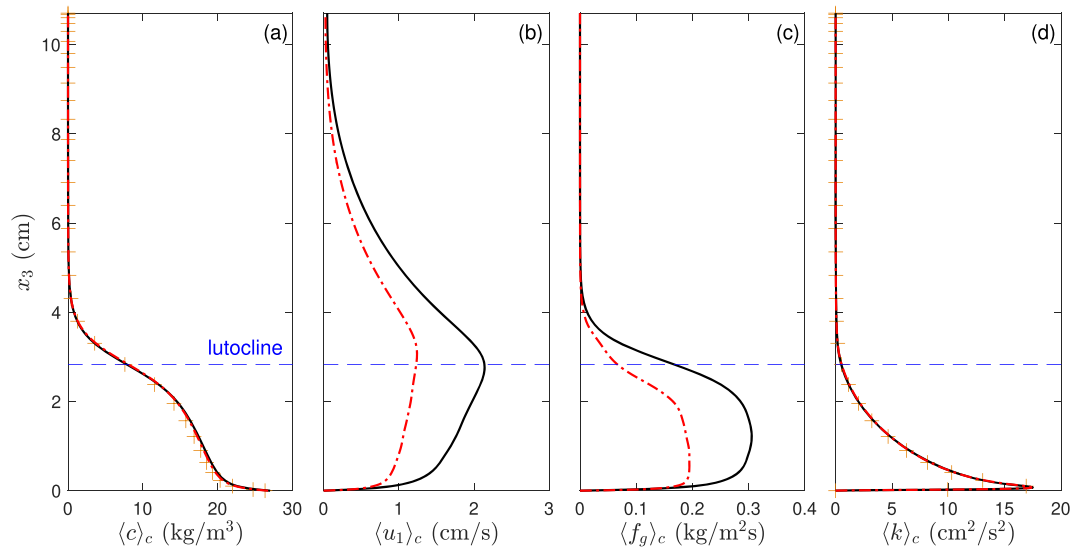


Figure 7. Vertical profiles of the time- and plane-averaged (a) mass concentration of sediment; (b) downslope current; (c) downslope mass flux of sediment; and (d) turbulence kinetic energy for Case 0 (brown crosses), Case 1 (red dash-dotted lines), and Case 2 (black lines).

the lutocline effectively separates the inner and outer regions. Moreover, above the lutocline in the outer region, the profiles of TKE are close to 0 which are also similar to typical turbidity currents (Meiburg & Kneller, 2010). In the present WSGF simulations, the time-averaged TKE at lutocline is only about 3% of its maximum in the inner region (Figure 7d).

3.2.2. Bottom Slope and Wave Boundary Layer

A key finding drawn from section 3.2.1 is that, by adding a gentle bottom slope of 0.005 to sediment-laden WBBL (relative to Case 0), a weak cross-shelf downslope current is generated. Although the wave direction relative to bottom slope plays an important role in determining the intensity of resulting downslope gravity current (Figure 7b), the suspended sediment load and turbulence intensity are both insensitive to the existence of bottom slope and thus the downslope current (Figures 7a and 7d).

The effect of the bottom slope on the modeled suspended sediment load is explained by examining the balance of sediment flux budget in bed-normal direction (equation (A1) in Appendix A), which consists of the turbulent suspension flux ($\langle u'_3 \phi' \rangle_c$), the settling flux ($-w \langle \phi \rangle_c$), and the diffusive/molecular sediment flux ($-K \partial \langle \phi \rangle_c / \partial x_3$). The flux budgets are computed here for all three cases, which are all very close to each other (Figure 8). In the region very near the bed ($x_3 < 0.5\Delta$), the flow is laminar and the upward diffusive flux from molecular diffusivity is responsible for suspending sediments. In the layer above the viscous sublayer ($x_3 > 1\Delta$) and below the lutocline ($x_3 < 16\Delta$), the settling flux is mainly balanced by the turbulent suspension flux, suggesting that the majority of sediment load in WSGF is maintained by the fluid turbulence in the WBBL. Thus, the similar vertical distribution of sediment mass concentration (Figure 7a) is consistent with the almost identical distribution of turbulence intensity (Figure 7d) for the three cases. Hence, we conclude that the similar concentration profile is mainly driven by the same and relatively large oscillatory velocity amplitude U_w ($U_w / \bar{U}_{gf} > 30$, see Table 2), while the presence of a mild bottom slope and the difference in wave direction have a minor effect. Approaching the lutocline, the diffusive flux begins to increase again around $x_3 = 10\Delta$, which is the result of flow turbulence attenuation by the sediment-induced stable density stratification. The local maximum of diffusive flux intercepts with the corresponding turbulent suspension flux at the location of lutocline, above which the molecular diffusive flux becomes dominant again in the flux budget. The existence of a local maximum in the molecular diffusive flux around the lutocline is regarded as a direct evidence of the two-layer like fine sediment transport system.

The small effect of bottom slope on the intensity of flow turbulence is explained by the time-averaged TKE budget of \bar{k} (equation (A2) in Appendix A). The production term in the budget consists of three components, which read $\langle \mathcal{P} \rangle_c = \langle \mathcal{P}_c \rangle_c + \langle \mathcal{P}_w \rangle_c + \langle \mathcal{P}_b \rangle_c$, corresponding to the production (or destruction) of \bar{k} , respectively, from the mean current, waves, and buoyancy. From Figure 9, it is evident that in all three cases, the dominant terms in the time-averaged TKE budget are the turbulence dissipation rate and the wave production. They

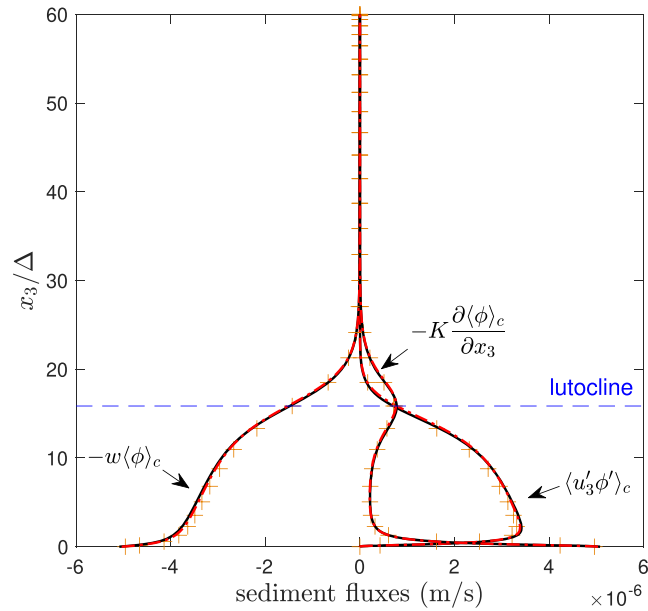


Figure 8. Flux budgets of sediment for Case 0 (brown crosses), Case 1 (red dash-dotted lines), and Case 2 (black lines).

balance with each other, except very near the bed, where turbulence production must decay to 0 at the bed. The other two sources, namely, the mean current and the buoyancy productions, contribute very little to the time-averaged TKE budget and are nearly 3 orders of magnitude smaller than the wave production (see the inset of Figure 9). In other words, the WBL gets most of the turbulence production from wave motion, which keeps the sediment load in suspension. Hence, the downslope gravity currents obtained in Case 1 and Case 2 are clearly wave-supported. Since the dominant terms in the energy budget ($\langle \varepsilon \rangle_c$ and $\langle \mathcal{P}_w \rangle_c$) are similar for all three cases, it is straightforward to understand that the resulting time-averaged TKE profiles shown in Figure 7d are also similar. Moreover, the buoyancy production ($\langle \mathcal{P}_b \rangle_c$) in all three cases is negative, because the sediment-induced stable stratification dominates $\langle \mathcal{P}_b \rangle_c$, which attenuates flow turbulence. This implies that the simulated WSGFs are not self-sustaining. The profiles of $\langle \mathcal{P}_b \rangle_c$ in these cases are all close

to each other due to the similar suspended sediment loads (Figure 7a). There is a notable difference in production due to mean current ($\langle \mathcal{P}_c \rangle_c$), because the wave direction affects the current velocity in WSGF. However, the magnitude of $\langle \mathcal{P}_c \rangle_c$ is very small when compared to that of $\langle \mathcal{P}_w \rangle_c$ and it has negligible effect on the overall plane- and time-averaged TKE budget.

3.3. WSGF Mechanics and the Role of Waves

3.3.1. Cross-Shelf Current Driven by Downslope Gravity

As shown in section 3.2, the presence of a gentle bottom slope leads to downslope gravity currents with a magnitude of a few cm/s. Importantly, the magnitude of the downslope gravity current is dependent on the wave direction. The reasoning process of the effect of wave direction begins with the momentum flux balance in the bed-normal direction (see the derivation of equation (A8) in Appendix A). Integrating equation (A8) again from 0 to x_3 and applying the no-slip bottom boundary condition, we obtain an explicit expression of the downslope current

$$\langle u_1 \rangle_c = \frac{1}{\nu} \left(\int_0^{x_3} \langle u'_1 u'_3 \rangle_c dx'' + Rgn_1 \int_0^{x_3} \int_{x''}^{L_3} \langle \phi \rangle_c dx' dx'' \right), \quad (19)$$

where x' and x'' are dummy variables. From equation (19), it is clear that the downslope current is determined by the vertically integrated time-averaged Reynolds stress (first term on RHS) and the strength

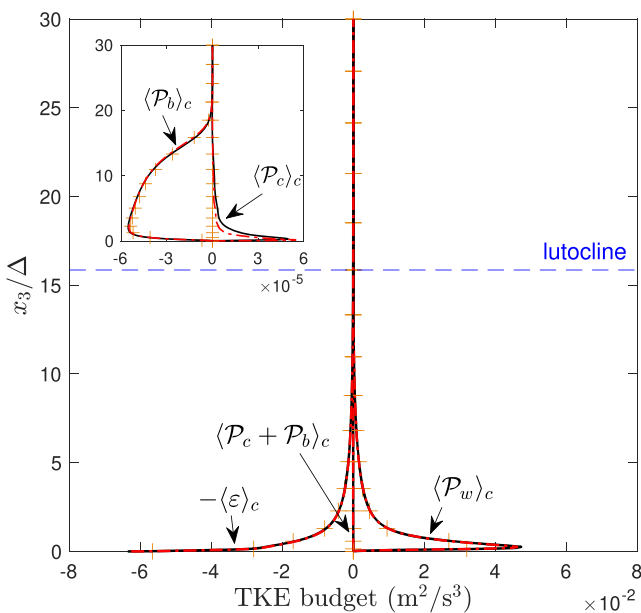


Figure 9. TKE budgets of the flow for Case 0 (brown crosses), Case 1 (red dash-dotted lines), and Case 2 (black lines).

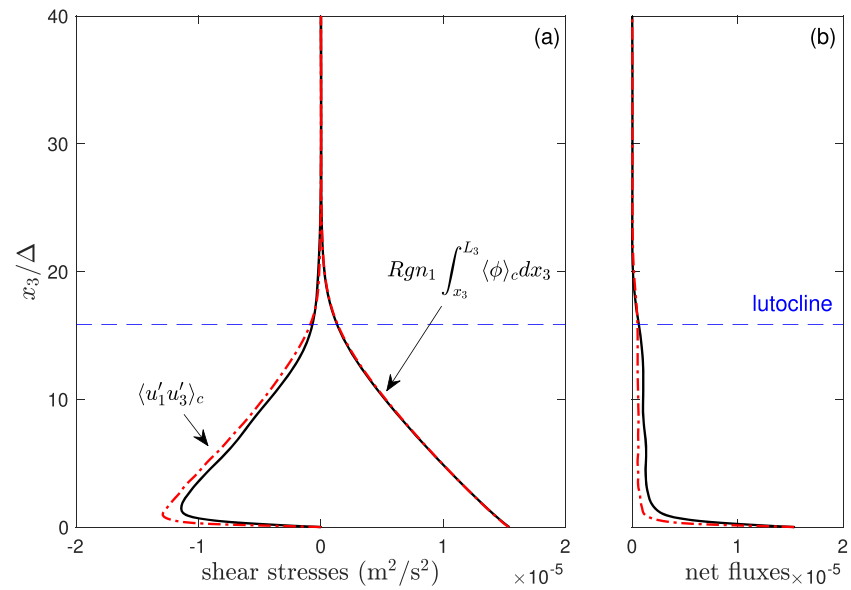


Figure 10. (a) Components in momentum flux balance in the bed-normal direction. (b) Net fluxes for Case 1 (red dash-dotted lines) and Case 2 (black lines).

of downslope driving force (last term on RHS). As it has been shown in previous sections that for Case 1 and Case 2, the concentration profiles are similar, regardless of wave direction. Therefore, equation (19) essentially indicates that the wave direction must affect the intensity of downslope gravity current through modifying the time-averaged Reynolds shear stress $\langle u'_1 u'_3 \rangle_c$.

As shown in Figure 10a for the balance of momentum flux (equation (A8)), the vertical profiles due to downslope buoyancy flux for the two cases are almost identical and the downslope driving forces associated with wave direction are very similar. On the other hand, we observe a notable difference in the vertical profiles of the time-averaged Reynolds shear stress $\langle u'_1 u'_3 \rangle_c$. When wave direction is parallel to the slope (and downslope gravity current), there exists a stronger time-averaged Reynolds shear stress to balance the downslope buoyancy flux. Therefore, the resulting net momentum flux on the left-hand side of equation (A8) becomes smaller. Figure 10b shows the net momentum fluxes and it is evident that for Case 1 with waves parallel to the downslope current, the net momentum flux is about 50% smaller than that of Case 2. This explains why the resulting WSGF speed for Case 1 is about a factor of 2 smaller (Table 2). Note from Figure 10 that the momentum fluxes associated with each term on the RHS of equation (A8) are about a factor of 8 greater than the net momentum flux. Therefore, we realize that a 10% difference in the time-averaged Reynolds shear stress $\langle u'_1 u'_3 \rangle_c$ due to wave direction can lead to almost a factor of 2 difference in the net momentum flux and hence the resulting downslope currents.

The dynamics of WSGF represented by the present simulations is not straightforward. Essentially, one needs to recognize that WSGF is a “small” magnitude time-averaged gravity current (a few cm/s) generated by suspended sediments, which are sustained by “large” magnitude of wave velocity (about 50 cm/s). Therefore, with the present high resolution numerical simulations for different scenarios, we can extract the difference and similarity in the momentum and turbulence energy balances to gain insight into WSGF dynamics.

3.3.2. Dependence on Wave-Induced Fluid Turbulence

According to the analysis of time-averaged TKE budget equation in section 3.2.2, the WSGFs obtained from the present simulations are sustained by persistent wave motions. To intuitively demonstrate this important feature, simulations of Case 1 and Case 2 are continued for another 20 wave periods from time $t_0 = 60T_w$ with a dampened wave forcing (equation (10)). In this study, we specify $\gamma = -0.044$ Hz in order to obtain a sufficient but gradual decay of the wave motions within about six wave periods (see Figure 11a). It is evident that the fluid turbulence responds rapidly with respect to the wave motion. The instantaneous plane-averaged TKE profiles indicate that turbulence is almost completely dissipated within first three damped waves (Figure 11d). The domain-averaged sediment concentrations show a milder decay than plane-averaged TKE,

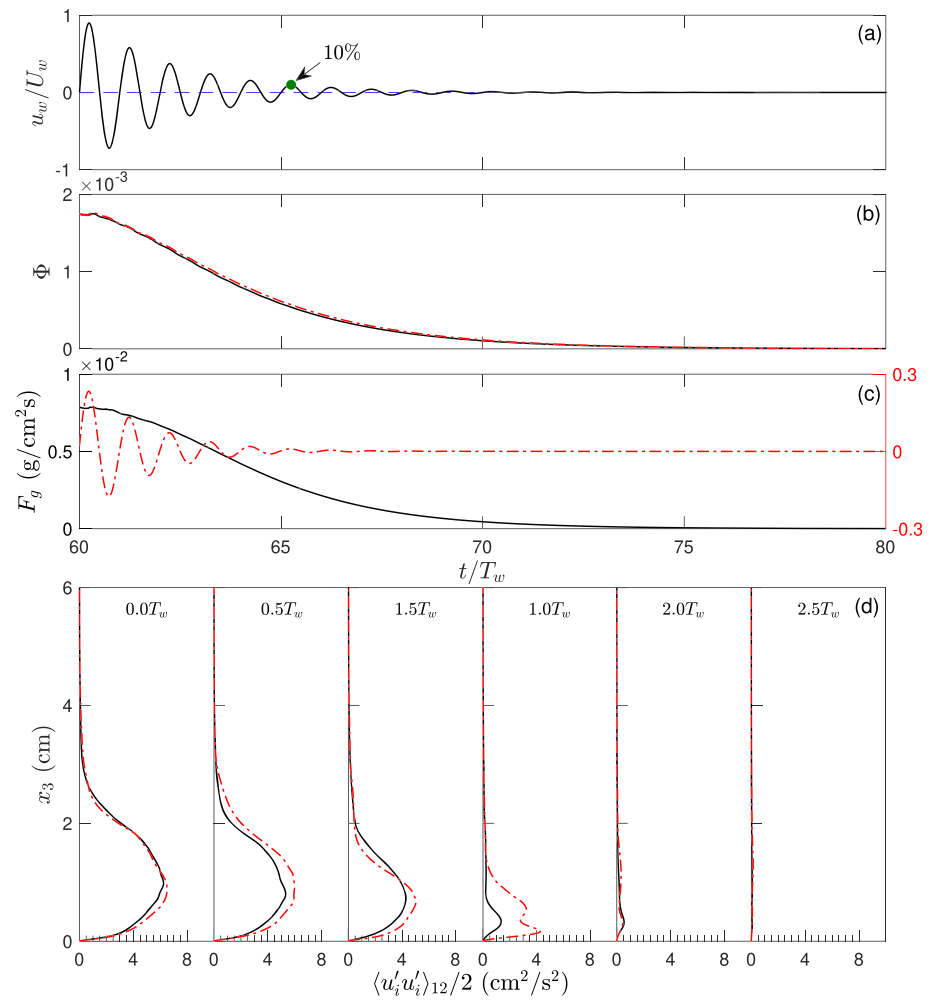


Figure 11. Time history of the (a) damped free-stream velocity; (b) domain-averaged volumetric concentration of sediment; and (c) domain-averaged mass transport rate of sediment in downslope direction. (d) Instantaneous profiles of turbulence kinetic energy at time $t - t_0 = [0.0, 0.5, 1.0, 1.5, 2.0, 2.5] T_w$ for Case 1 (red dash-dotted lines) and Case 2 (black lines).

although almost all the sediments are deposited within 15 wave periods after the wave forcing has been attenuated.

To be specific, at $t - t_0 = 5.25T_w$, more than 30% of sediment is still suspended in the computational domain and it is until $t - t_0 = 15T_w$, the domain loses most (99%) of the suspended sediment (Figure 11b). The longer retention time of suspended sediment in the computational domain is explained by the small settling velocity of sediment (or small fall parameter) used in these simulations. Due to the decay of suspended sediment load in the domain, the corresponding downslope sediment fluxes F_g also decrease accordingly (Figure 11c). This is most clear by inspecting the F_g of Case 2, in which the downslope sediment flux is perpendicular to the wave motion. The downslope sediment flux decays as fast as the concentration and the WSGF is terminated within $15T_w$.

4. Discussion

4.1. Comparison With Observations

Clearly from section 3.2, adding a gentle bottom slope to sediment-laden WBBL leads to WSGFs. For Case 1, in which the wave direction is parallel to the downslope direction, we obtain the peak downslope velocity of 1.2 cm/s near the location of lutocline. This value is about 50% larger than that reported by Ozdemir (2016) of 0.8 cm/s, which uses a prescribed suspended sediment load near flow carrying capacity. This suggests that WSGF dynamics are dependent on the exchange of sediment with the bed. However, the resulting

cross-shelf current speed is still smaller than most of the field observed data. For instance, through extrapolation of velocity to the WBBL, Traykovski et al. (2000) suggested a downslope current speed of about 10 cm/s. In later field observations, collected at the Po prodelta, the peak downslope velocity of an energetic WSGF event was reported to be around 5 cm/s (Traykovski et al., 2007). Jaramillo et al. (2009) reported 3 ~ 5 cm/s for WSGF events observed at Atchafalaya shelf. Through indirect estimate of the sediment flux budget, Hale and Ogston (2015) obtained lower values of WSGF velocity of 2 ~ 3 cm/s on the continental shelf offshore of the Waipaoa River. However, the shelf slope in these later two field sites is milder (~ 0.003) than that reported by Traykovski et al. (2000). A recent measurement of the downslope current speed of WSGF by Flores et al. (2018) in a mixed sediment site also suggested a speed of 5 cm/s. A more careful comparison of our model results with these field data indicates that the main reason that the present simulations predict lower downslope gravity current speed is because the computed near-bed sediment mass concentration is only about 26 kg/m³ (g/L). This mass concentration is about a factor of 2 smaller than field-reported values during WSGF events. According to Cheng et al. (2015), further reducing the critical shear stress of erosion to increase the suspended sediment load while keeping all the other parameters the same will cause flow laminarization. In other words, for the present wave intensity and the flat bed setup, WBBL is transitionally turbulent and the suspended sediment load cannot be further enhanced beyond its sediment-carrying capacity.

We have investigated the effect of wave direction on WSGF. Results suggest the wave direction plays an important role in determining the intensity of resulting downslope gravity current, although the sediment load (Figure 7a) and turbulence intensity (Figure 7d) are both insensitive to the wave direction. As a result, having waves perpendicular to the downslope direction only increases the peak downslope gravity current velocity to 2.1 cm/s, which is still on the low side when compared to observed flow velocities. Overall, our simulation results imply that other factors, such as the presence of small bedforms (Traykovski et al., 2015) and ambient currents (Ma et al., 2008), should be investigated in the future to understand their roles in enhancing the suspended sediment load and the resulting downslope current speed. Moreover, the present study ignores the flocculation process and the hindered settling of fine sediment. We simply specify a constant settling velocity of 0.5 mm/s, which is comparable to commonly accepted value for fine sediment (Hill et al., 2000). The effects of flocculation and hindered settling on the settling velocity in WBBL and the resulting WSGF dynamics also warrant future investigation. Finally, the present study assumes a perfect symmetric wave motion while in reality, wave velocity skewness may also play a role.

4.2. Parameterization of WSGFs

The parameterization of WSGFs is necessary in quantifying and predicting the cross-shelf fine sediment transport (Scully et al., 2003; Wright et al., 2001). One of the most common parameterization methods is formulated through the balance between the wave-averaged bottom friction and the sediment-induced downslope gravitational force. The momentum balance in downslope direction presented in equation (A7) is completely consistent with this classical force balance, commonly called the Chezy equation (Wright et al., 2001)

$$B \sin \theta = C_D U_g U_{\max}, \quad (20)$$

where C_D is a nondimensional bottom drag coefficient, U_g is depth-averaged downslope velocity, U_{\max} is the magnitude of velocity at top of the bottom boundary layer. The depth-integrated buoyancy anomaly is represented by B , which reads

$$B = gR \int_0^{L_3} \phi dx_3, \quad (21)$$

The idea behind the parameterization equation (20) is that the averaged downslope velocity of gravity current U_g can be calculated using the depth-integrated buoyancy anomaly B and U_{\max} (which can be estimated from field measured data), when a reasonable value of drag coefficient C_D is specified.

The Chezy formulation was originally developed for parameterizing autosuspending turbidity currents and there was no ambiguity in estimating U_{\max} using U_g (Meiburg & Kneller, 2010). The autosuspension criterion $\beta = w/U_g \theta$ proposed by Parker (1982) is calculated for WSGF here (see Table 3). Both cases show $\beta \gg 1$ and thus WSGFs are distinct from the autosuspending turbidity currents. As a result, the parameter U_{\max} is well approximated by U_w rather than U_g , since $U_g \ll U_w$. Moreover, the present simulation results indicate

Table 3
Parameterization of WSGFs

Case	U_w (cm/s)	U_g (cm/s)	B (cm ² /s ²)	Ri_{cr}	β	C_D
1	56	0.59	30.73	9.80×10^{-3}	30.39	4.67×10^{-3}
2	56	0.96	30.82	9.83×10^{-3}	18.66	2.88×10^{-3}

that the bottom drag coefficient is 0.0047 for waves that propagate in the cross-shelf direction (Case 1), see Table 3. This value is on the high end of C_D reported by the review paper of Wright and Friedrichs (2006), who suggested $C_D = 0.002 \sim 0.005$. This value is also consistent with the value of $C_D = 0.006$ suggested by the recent turbulence-resolving numerical investigation of Ozdemir (2016). It should be noted that in most of the field studies, C_D is estimated to be around 0.003 (Flores et al., 2018; Hale & Ogston, 2015) or lower (Traykovski et al., 2000, 2007). Interestingly, by considering the direction of waves are in along-shelf direction (Case 2), we obtain significantly lower C_D of 0.0029. In other words, the nearly factor of 2 variability of C_D reported in the field observation between $C_D = 0.003 \sim 0.005$ may be explained by the effect of wave direction. The enhanced drag coefficient when the waves are in the same direction of the downslope current is due to increased time-averaged Reynolds shear stress, as presented in Figure 10. Here, it is also useful to point out that this feature is consistent with the well-known “apparent roughness” concept (Grant & Madsen, 1986). This concept indicates that a more significant roughness (larger than the physical roughness of the bed) is experienced by the current when superimposed a wave motion, due to the enhanced turbulence in the WBBL. As discussed in detail by Grant and Madsen (1986), this enhanced roughness depends on wave direction and it is maximized when waves are in the same direction with the current.

Historically, there exists a discrepancy in the estimation of B for WSGF modeling (Parsons et al., 2009). A widely used idea is to estimate the buoyancy anomaly based on velocity magnitude U_{max} (or U_w for our cases) and an empirical critical Richardson number Ri_{cr} as $B = Ri_{cr} U_{max}^2$. By assuming that the WBBL maintains its sediment-carrying capacity, Ri_{cr} is suggested to be 0.25 (Scully et al., 2002; Wright et al., 2001; Wright & Friedrichs, 2006). However, recent field measurements (Hale & Ogston, 2015; Traykovski et al., 2015), laboratory experiments (Lamb & Parsons, 2005) and numerical studies (Ozdemir, 2016) suggest that the Ri_{cr} of WSGF is much lower than the widely used value of 0.25. As summarized in Table 3, the present simulations give an empirical critical Richardson number Ri_{cr} around 0.01, regardless of wave direction. This value is significantly smaller than 0.25, but it is consistent with recent field observations of Flores et al. (2018), who reported $Ri_{cr} = 0.01$ and laboratory experiments of Lamb and Parsons (2005) showing $Ri_{cr} = 0.013$ where sediment concentration is directly measured. Although there exist larger uncertainties in earlier field measurements, many WSGF events are observed in the field to occur at Ri_{cr} much lower than 0.25 (Traykovski et al., 2007). It should be pointed out that a sediment-carrying capacity equivalent to $Ri_{cr} = 0.25$ is often observed in fully turbulent flow, such as turbidity current or tidal boundary layer (Trowbridge & Kineke, 1994). Our numerical investigation indicates that for WSGF generated at Stokes Reynolds number around 1,000, the resulting WBBL is transitionally turbulent with a lower carrying capacity and the corresponding Ri_{cr} is one order of magnitude smaller than 0.25.

5. Conclusions

Turbulence-resolving numerical simulations of wave-supported sediment-driven gravity flows in energetic wave condition at a slope of 0.005 over a flat bed are reported in this study. By allowing sediments to be freely eroded from and deposited to the bottom, we address our research objectives by investigating the relationship between the wave boundary layer turbulence, the suspended sediment load, and the resulting downslope gravity current in response to wave directions. Through the intrawave evolution of bed shear stresses, coherent turbulent structures, and sediment concentration and turbulence statistics, we confirm that the present problem belongs to the category of transitionally turbulent flow. While the transitionally turbulent WBBL can support a maximum sediment load approaching 30 kg/m³ which leads to sufficient sediment-induced buoyancy anomaly to drive the downslope gravity flow, as far as the maximum sediment load and leading-order turbulence statistics are concerned, the effect of wave direction is negligible. The reason behind this finding is explained through the time- and plane-averaged sediment mass flux budget and the TKE budget. Simulation results reveal that the maximum downslope gravity current speed is around 2 cm/s when the wave direction is perpendicular to the downslope direction. However, as the waves become

parallel to the slope, the resulting downslope current intensity and hence the downslope sediment flux are reduced by a factor of 2. From analyzing the time- and plane-averaged momentum flux balance, we conclude that the wave direction changes the time-averaged Reynolds stress experienced by the downslope current. Hence, the mechanism is consistent with the classical apparent roughness concept.

Simulation results are further used to examine the drag coefficient C_D and the empirical critical Richardson number Ri_{cr} for the parameterization of WSGFs. The drag coefficient C_D is found to be around 0.005 for waves are in along-shelf direction while it reduces to about 0.003 when waves are in cross-shelf direction. Simulation results also indicate that for the present flat bed condition driven solely by the wave motions in a transitionally turbulent WBBL, the maximum sediment load is limited and the resulting Ri_{cr} is significantly lower than 0.25. For some field observations reporting WSGF events occur at higher carrying capacity (and possibly more intense downslope gravity current), the present simulations imply that other processes, such as the presence of ambient current and bedforms, may play important roles.

Appendix A: Derivation of Budget/Balance Equations

We first discuss the mass balance equation for the sediment volumetric flux in bed-normal direction. After applying the triple decomposition (section 2.5) in equation (6) and taking the time- and plane-averaging on both sides, the following budget equation of sediment volumetric flux is obtained after the integration of x_3 in the bed-normal direction (Nelson & Fringer, 2018)

$$\langle u'_3 \phi' \rangle_c - w \langle \phi \rangle_c - K \frac{\partial \langle \phi \rangle_c}{\partial x_3} = 0, \quad (A1)$$

where the three components on left-hand side are the turbulent suspension flux, settling flux, and diffusive (molecular) sediment flux, respectively.

The time-averaged TKE budget equation is also used in this study, which reads (Reynolds & Hussain, 1972)

$$\frac{\overline{Dk}}{Dt} + \nabla \cdot T' = \langle \mathcal{P}_c \rangle_c + \langle \mathcal{P}_w \rangle_c + \langle \mathcal{P}_b \rangle_c - \langle \epsilon \rangle_c, \quad (A2)$$

where $\overline{D}/Dt = \partial/\partial t + \bar{u}_j \partial/\partial x_j$ and ϵ denotes the turbulence dissipation rate, which reads

$$\epsilon = \nu \frac{\partial u'_i}{\partial x_j} \frac{\partial u'_i}{\partial x_j}. \quad (A3)$$

The terms $\langle \mathcal{P}_c \rangle_c$, $\langle \mathcal{P}_w \rangle_c$ and $\langle \mathcal{P}_b \rangle_c$ on the RHS of equation (A2) represent the production (or destruction) of \bar{k} , respectively, from the mean current, waves, and buoyancy, which are written as

$$\mathcal{P}_c = -\overline{u'_i u'_j} \frac{\partial \bar{u}_i}{\partial x_j}, \quad (A4)$$

$$\mathcal{P}_w = -\langle u'_i u'_j \rangle_p \frac{\partial \langle u_i \rangle_w}{\partial x_j}, \quad (A5)$$

$$\mathcal{P}_b = Rgn_i \phi' u'_i. \quad (A6)$$

Finally, the remaining terms in the plane- and time-averaged TKE budget equation (A2) are represented by $\nabla \cdot T'$.

For addressing the role of downslope gravity and wave direction in WSGF, the balance equation of momentum flux in bed-normal direction is also needed. The derivation begins with the time- and plane-averaged momentum equation in the downslope direction. This equation is derived from equation (2) after applying the time- and plane-averaging on both sides of it, which reads

$$\nu \frac{\partial^2 \langle u_1 \rangle_c}{\partial x_3^2} - \frac{\partial \langle u'_1 u'_3 \rangle_c}{\partial x_3} \equiv \frac{\partial \langle \tau \rangle_c}{\partial x_3} = -Rgn_1 \langle \phi \rangle_c, \quad (A7)$$

where $\langle \tau \rangle_c$ is the total shear stress including the time- and plane-averaged viscous and Reynolds shear stresses. The above equation is consistent with the argument by Parsons et al. (2009) that the basic dynamics of WSGF are governed by the force balance in the cross-shelf direction between the downslope gravitational force (last term) and the vertical distribution of the total shear stress in the water column ($\partial \langle \tau \rangle_c / \partial x_3$). By vertically integrating equation (A7) from x_3 to the top of the computational domain and applying the free-slip boundary condition on $x_3 = L_3$, we obtain the balance equation of momentum flux in the bed-normal direction as

$$v \frac{\partial \langle u_1 \rangle_c}{\partial x_3} = \langle u_1' u_3' \rangle_c + Rgn_1 \int_{x_3}^{L_3} \langle \phi \rangle_c dx', \quad (\text{A8})$$

where x' is a dummy variable. A good agreement of the above momentum flux balance in present simulations has been found. The momentum flux balance equation (A8) combined with the sediment flux budget equation (A1) represents the dual role of wave-induced fluid turbulence in WSGF: providing energy to keep sediments in suspension which further forces the downslope current, and contributing to the resistance (the component of Reynolds stress in the total shear stress) against the downslope driving force in the bottom boundary layer.

Acknowledgments

This study is supported by NSF (OCE-1537231 and OCE-1924532) and Office of Naval Research (N00014-17-1-2796). Numerical simulations presented in this study were carried out using the Mills and Canviness clusters at University of Delaware, and the SuperMIC cluster at Louisiana State University via XSEDE (TG-OCE100015). Z. Cheng would like to express thanks for the support of a postdoctoral scholarship from Woods Hole Oceanographic Institution. The source code and the case setup to reproduce the same results are publicly available via the repository maintained by GitHub: <https://github.com/yueliangyi/TURBID> (source code) and https://github.com/yueliangyi/TURBID/tree/master/spike/wave_supported_gravity_flow (case setup), respectively.

References

- Arakawa, A., & Lamb, V. R. (1981). A potential enstrophy and energy conserving scheme for the shallow water equations. *Monthly Weather Review*, *109*(1), 18–36.
- Balachandar, S., & Eaton, J. K. (2010). Turbulent dispersed multiphase flow. *Annual Review of Fluid Mechanics*, *42*(1), 111–133.
- Canuto, C., Hussaini, M. Y., Quarteroni, A., & Zang, T. A. (1988). *Spectral methods in fluid dynamics*. Berlin: Springer-Verlag.
- Cheng, Z., Yu, X., Hsu, T. J., Ozdemir, C. E., & Balachandar, S. (2015). On the transport modes of fine sediment in the wave boundary layer due to resuspension/deposition: A turbulence-resolving numerical investigation. *Journal of Geophysical Research: Oceans*, *120*, 1918–1936. <https://doi.org/10.1002/2014JC010623>
- Chorin, A. J. (1968). Numerical solution of the Navier-Stokes equations. *Mathematics of Computation*, *22*(104), 745–745.
- Cortese, T. A., & Balachandar, S. (1995). High performance spectral simulation of turbulent flows in massively parallel machines with distributed memory. *The International Journal of Supercomputer Applications and High Performance Computing*, *9*(3), 187–204. <https://doi.org/10.1177/109434209500900302>
- Ferry, J., Rani, S. L., & Balachandar, S. (2003). A locally implicit improvement of the equilibrium Eulerian method. *International Journal of Multiphase Flow*, *29*(6), 869–891.
- Flores, R. P., Rijnsburger, S., Meirelles, S., Horner-Devine, A. R., Souza, A. J., Pietrzak, J. D., et al. (2018). Wave generation of gravity-driven sediment flows on a predominantly sandy seabed. *Geophysical Research Letters*, *45*, 7634–7645. <https://doi.org/10.1029/2018GL077936>
- Geyer, W. R., Hill, P., Milligan, T., & Traykovski, P. (2000). The structure of the Eel River plume during floods. *Continental Shelf Research*, *20*(16), 2067–2093.
- Grant, W. D., & Madsen, O. S. (1986). The continental-shelf bottom boundary layer. *Annual Review of Fluid Mechanics*, *18*(1), 265–305.
- Hale, R. P., & Ogston, A. S. (2015). In situ observations of wave-supported fluid-mud generation and deposition on an active continental margin. *Journal of Geophysical Research: Earth Surface*, *120*, 2357–2373. <https://doi.org/10.1002/2015JF003630>
- Harris, C. K., Traykovski, P. A., & Geyer, W. R. (2005). Flood dispersal and deposition by near-bed gravitational sediment flows and oceanographic transport: A numerical modeling study of the Eel River shelf, northern California. *Journal of Geophysical Research*, *110*, C09025. <https://doi.org/10.1029/2004JC002727>
- Harris, C. K., & Wiberg, P. (2002). Across-shelf sediment transport: Interactions between suspended sediment and bed sediment. *Journal of Geophysical Research*, *107*(C1), 3008. <https://doi.org/10.1029/2000JC000634>
- Hill, P. S., Milligan, T. G., & Geyer, W. R. (2000). Controls on effective settling velocity of suspended sediment in the Eel River flood plume. *Continental Shelf Research*, *20*(16), 2095–2111.
- Hooshmand, A., Horner-Devine, A. R., & Lamb, M. P. (2015). Structure of turbulence and sediment stratification in wave-supported mud layers. *Journal of Geophysical Research: Oceans*, *120*, 2430–2448. <https://doi.org/10.1002/2014JC010231>
- Jaramillo, S., Sheremet, A., Allison, M. A., Reed, A. H., & Holland, K. T. (2009). Wave-mud interactions over the muddy Atchafalaya subaqueous clinof orm, Louisiana, United States: Wave-supported sediment transport. *Journal of Geophysical Research*, *114*, C04002. <https://doi.org/10.1029/2008JC004821>
- Jensen, B. L., Sumer, B. M., & Fredsoe, J. (1989). Turbulent oscillatory boundary layers at high Reynolds numbers. *Journal of Fluid Mechanics*, *206*, 265–297.
- Kim, J., Moin, P., & Moser, R. (1987). Turbulence statistics in fully developed channel flow at low Reynolds number. *Journal of Fluid Mechanics*, *177*, 133–166.
- Lamb, M. P., & Parsons, J. D. (2005). High-density suspensions formed under waves. *Journal of Sedimentary Research*, *75*(3), 386–397.
- Ma, Y., Wright, L. D., & Friedrichs, C. T. (2008). Observations of sediment transport on the continental shelf off the mouth of the Waipau River, New Zealand: Evidence for current-supported gravity flows. *Continental Shelf Research*, *28*(4–5), 516–532.
- Meiburg, E., & Kneller, B. (2010). Turbidity currents and their deposits. *Annual Review of Fluid Mechanics*, *42*(1), 135–156.
- Nelson, K. S., & Fringer, O. B. (2018). Sediment dynamics in wind wave-dominated shallow-water environments. *Journal of Geophysical Research: Oceans*, *123*, 6996–7015. <https://doi.org/10.1029/2018JC013894>
- Nittrouer, C. A., & Wright, L. D. (1994). Transport of particles across continental shelves. *Reviews of Geophysics*, *32*(1), 85–113.
- Ogston, A. S. S., Cacchione, D. A. A., Sternberg, R. W. W., & Kineke, G. C. C. (2000). Observations of storm and river flood-driven sediment transport on the Northern California continental shelf. *Continental Shelf Research*, *20*(16), 2141–2162.
- Ozdemir, C. E. (2016). Turbulence-resolving, two-phase flow simulations of wave-supported gravity flows: A conceptual study. *Journal of Geophysical Research: Oceans*, *121*, 8849–8871. <https://doi.org/10.1002/2016JC012061>
- Ozdemir, C. E., Hsu, T.-J., & Balachandar, S. (2010). A numerical investigation of fine particle laden flow in an oscillatory channel: The role of particle-induced density stratification. *Journal of Fluid Mechanics*, *665*, 1–45.

- Parker, G. (1982). Conditions for the ignition of catastrophically erosive turbidity currents. *Marine Geology*, *46*(3-4), 307–327. [https://doi.org/10.1016/0025-3227\(82\)90086-X](https://doi.org/10.1016/0025-3227(82)90086-X)
- Parsons, J. D., Friedrichs, C. T., Traykovski, P. A., Mohrig, D., Imran, J., Syvitski, J. P. M., et al. (2009). The mechanics of marine sediment gravity flows, *Continental margin sedimentation* (pp. 275–337): Blackwell Publishing Ltd.
- Pekurovsky, D. (2012). P3DFFT: A framework for parallel computations of Fourier transforms in three dimensions. *SIAM Journal on Scientific Computing*, *34*(4), C192–C209.
- Peyret, R. (2002). *Spectral methods for incompressible viscous flow*. New York: Springer-Verlag.
- Reynolds, W. C., & Hussain, A. K. M. F. (1972). The mechanics of an organized wave in turbulent shear flow. Part 3. Theoretical models and comparisons with experiments. *Journal of Fluid Mechanics*, *54*(2), 263–288.
- Sanford, L. P. (2008). Modeling a dynamically varying mixed sediment bed with erosion, deposition, bioturbation, consolidation, and armoring. *Computers & Geosciences*, *34*(10), 1263–1283.
- Sanford, L. P., & Maa, Jerome P.-Y. (2001). A unified erosion formulation for fine sediments. *Marine Geology*, *179*(1-2), 9–23.
- Scully, M. E. E., Friedrichs, C. T. T., & Wright, L. D. D. (2002). Application of an analytical model of critically stratified gravity-driven sediment transport and deposition to observations from the eel river continental shelf, northern California. *Continental Shelf Research*, *22*(14), 1951–1974.
- Scully, M. E. E., Friedrichs, C. T. T., & Wright, L. D. D. (2003). Numerical modeling of gravity-driven sediment transport and deposition on an energetic continental shelf: Eel River, northern California. *Journal of Geophysical Research*, *108*(C4), 3120. <https://doi.org/10.1029/2002JC001467>
- Shringarpure, M., Cantero, M. I., & Balachandar, S. (2012). Dynamics of complete turbulence suppression in turbidity currents driven by monodisperse suspensions of sediment. *Journal of Fluid Mechanics*, *712*, 384–417.
- Soulsby, R. L., Manning, A. J., Spearman, J., & Whitehouse, R. J. S. (2013). Settling velocity and mass settling flux of flocculated estuarine sediments. *Marine Geology*, *339*, 1–12.
- Traykovski, P., Geyer, W. R. R., Irish, J. D. D., & Lynch, J. F. F. (2000). The role of wave-induced density-driven fluid mud flows for cross-shelf transport on the Eel River continental shelf. *Continental Shelf Research*, *20*(16), 2113–2140.
- Traykovski, P., Trowbridge, J., & Kineke, G. (2015). Mechanisms of surface wave energy dissipation over a high-concentration sediment suspension. *Journal of Geophysical Research: Oceans*, *120*, 1638–1681. <https://doi.org/10.1002/2014JC010245>
- Traykovski, P., Wiberg, P. L. L., & Geyer, W. R. R. (2007). Observations and modeling of wave-supported sediment gravity flows on the Po delta and comparison to prior observations from the Eel shelf. *Continental Shelf Research*, *27*(3-4), 375–399.
- Trowbridge, J. H., & Kineke, G. C. (1994). Structure and dynamics of fluid muds on the Amazon Continental Shelf. *Journal of Geophysical Research*, *99*(C1), 865. <https://doi.org/10.1029/93JC02860>
- Trowbridge, J., & Madsen, O. S. (1984). Turbulent wave boundary layers: 2. Second-order theory and mass transport. *Journal of Geophysical Research*, *89*(C5), 7999–8007. <https://doi.org/10.1029/JC089iC05p07999>
- Vittori, G., & Verzicco, R. (1998). Direct simulation of transition in an oscillatory boundary layer. *Journal of Fluid Mechanics*, *371*, 207–232.
- Williamson, J. H. H. (1980). Low-storage Runge-Kutta schemes. *Journal of Computational Physics*, *35*(1), 48–56.
- Wright, L. D. D., & Friedrichs, C. T. T. (2006). Gravity-driven sediment transport on continental shelves: A status report. *Continental Shelf Research*, *26*(17), 2092–2107.
- Wright, L. D. D., Friedrichs, C. T. T., Kim, S. C. C., & Scully, M. E. E. (2001). Effects of ambient currents and waves on gravity-driven sediment transport on continental shelves. *Marine Geology*, *175*(1-4), 25–45.
- Wright, L. D. D., & Nittrouer, C. A. A. (1995). Dispersal of river sediments in coastal seas: Six contrasting cases. *Estuaries*, *18*(3), 494.
- Yue, L., Cheng, Z., & Hsu, T.-J. (2019). Turbid: A turbulence-resolving numerical model for simulating bottom boundary layer and fine sediment transport: Center for Applied Coastal Research, Department of Civil and Environmental Engineering, University of Delaware.
- Zhou, J., Adrian, R. J., Balachandar, S., & Kendall, T. M. (1999). Mechanisms for generating coherent packets of hairpin vortices in channel flow. *Journal of Fluid Mechanics*, *387*, 353–396.